

# Structure Unbiased Adversarial Model for Medical Image Segmentation

Tianyang Zhang, Shaoming Zheng, Jun Cheng, Xi Jia, Joseph Bartlett, Huazhu Fu, Zhaowen Qiu, Jiang Liu and Jinming Duan

**Abstract**—Generative models have been widely proposed in image recognition to generate more images where the distribution is similar to that of the real images. It often introduces a discriminator network to discriminate original real data and generated data. However, such discriminator often considers the distribution of the data and did not pay enough attention to the intrinsic gap due to structure. In this paper, we reformulate a new image to image translation problem to reduce structural gap, in addition to the typical intensity distribution gap. We further propose a simple yet important Structure Unbiased Adversarial Model for Medical Image Segmentation (SUAM) with learnable inverse structural deformation for medical image segmentation. It consists of a structure extractor, an attention diffeomorphic registration and a structure & intensity distribution rendering module. The structure extractor aims to extract the dominant structure of the input image. The attention diffeomorphic registration is proposed to reduce the structure gap with an inverse deformation field to warp the prediction masks back to its original form. The structure rendering module is to render the deformed structure to an image with targeted intensity distribution. We apply the proposed SUAM on both optical coherence tomography (OCT), magnetic resonance imaging (MRI) and computerized tomography (CT) data. Experimental results show that the proposed method has the capability to transfer both intensity and structure distributions.

**Index Terms**—Generative adversarial network, Domain Gaps, medical image segmentation

## I. INTRODUCTION

MEDICAL image processing [1], [2] has been a hot topic in last few decades. Recently, deep learning based techniques have drawn lots of attention [3], [4]. These methods often assume that the training and test data follows the same distribution. However, domain gaps often exist among data from different sources, *e.g.*, the data from different hospitals or clinic centers are often captured by different machines with different models/parameter settings. In addition, as the imaging technology progresses, new machines are replacing the old ones. Therefore, the accumulated data even from the same hospital can have different distributions. It is obvious that re-collecting and labeling the required training data for each new

T. Zhang, X. Jia, J. Bartlett, and J. Duan are with the University of Birmingham, Birmingham, UK. (e-mail: TXZ009@student.bham.ac.uk; X.Jia.1@cs.bham.ac.uk; jxb1336@student.bham.ac.uk; j.duan@cs.bham.ac.uk). J. Duan is also a Fellow of the Alan Turing Institute, London. S. Zheng is with University of Pennsylvania, USA. (e-mail: shaoming@seas.upenn.edu). J. Cheng is with Institute for Infocomm Research, A\*STAR, Singapore. (e-mail: sam.j.cheng@gmail.com). H. Fu is with Institute of High Performance Computing, A\*STAR, Singapore. (e-mail: hzfu@ieee.org). Z. Qiu is with the NorthEast Forestry University, Harbin, China. (e-mail: qiuzyw@nefu.edu.cn). J. Liu is with the Southern University of Science and Technology, Shenzhen, China. (e-mail: liuj@sustech.edu.cn). The corresponding authors are Jun Cheng and Jinming Duan.

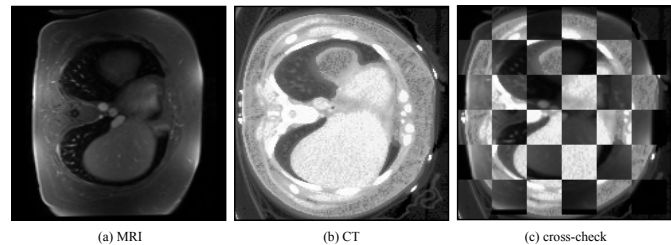


Fig. 1. Illustrations of domain gaps: (a) MRI chest image, (b) CT image, (c) cross-check image with affine transformation alignment.

device/model is too expensive and time consuming. Therefore, the effective use of labelled data from previous devices or settings is vital.

To solve this issue, transfer learning [5]–[7] is a possible way to map the data into a different space such that the domain gaps between source domain and target domain are minimized. A limitation of such an approach is that it often requires a re-training of the models. Moreover, the mapping to the different space may also lead to some information loss and is not necessarily optimised for the subsequent tasks. Recently, generative adversarial models are proposed to tackle this problem by transferring the intensity distributions from source to target domain and reducing the domain gaps. Previously, Chen *et al.* [8] proposed a MUNIT based model to transfer the intensity distribution of source dataset to the target dataset. Zhang *et al.* [9] proposed to generate new images by maintaining the main edges in the images. However, these methods overlooked the difference in structure statistics. The structure information captured using various imaging techniques can be different due to the nature of imaging principles. For instance, the curvatures of the objects of interest in images are largely affected by scales. Fig. 1 shows a pair of CT and MRI images as well as their cross-check image which highlights the misalignment between the aligned paired images. We refer such domain gap as structure gap.

The problem of domain gaps is formulated in Fig. 2. As shown, the intensity differences can be reduced to narrow the distance between the two distributions. However, the structural gap cannot be completely removed due to the presence of the structure difference, which limits the efficacy of the translation-based GANs. In this paper, we propose a simple yet important structure unbiased adversarial approach to overcome the above issue. It translates the test data into the training data domain such that both structures and intensities are similar. With this translation, it is expected that the models trained

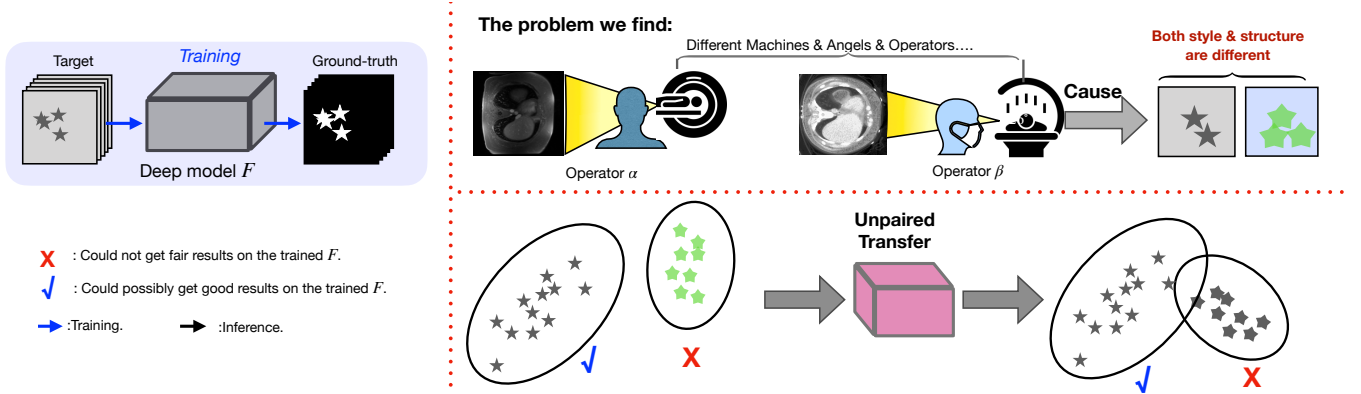


Fig. 2. Problem Formulation:  $F$  denotes a trained deep model in the target domain, while it usually does not work well in the source domain due to the domain shifts. The existing GAN based translation methods could ease the burden caused by different intensities to trained networks. However, in many cases (collected from different machines or under different modalities), structures and shapes are also different. This makes the training of the discriminator challenging.

from the training data would fit to the translated test data. Moreover, we also propose an inverse deformation field to warp the segmentation result back to its original domain, which is an essential step to avoid inaccurate segmentation results due to structure deformation.

The main contributions of the paper are summarized as follows:

- We identify a new simple yet important image to image translation problem which aims to reduce domain gaps associated with both structures and intensity distributions.
- We propose SUAM to tackle this domain gap problem. Our method includes three distinctive parts including dominant structure extractor, attention based diffeomorphic registration, and structure and intensity distribution rendering mapping. For diffeomorphic registration, we propose a method to compute inverse deformation fields, which are essential for the downstream segmentation task.
- We conduct extensive experimental results on retinal OCT and chest CT & MRI datasets and show that the proposed method is able to transfer both structures and intensity distributions effectively with improved subsequent segmentation accuracy.

The rest of the paper is organized as follows. Section II reviews the related work. Section III introduces the proposed SUAM including the structure extractor, the attention diffeomorphic registration, the structure rendering module and the losses computation. In Section IV, we introduce the experimental results. The last section concludes the paper.

## II. RELATED WORKS

### A. Generative Adversarial Networks (GANs)

GANs [10], [11] are originally proposed to generate images from random inputs in an un-conditional manner. It contains a generator and a discriminator where the generator aims to output samples to be indistinguishable from the training samples while the discriminator tries to differentiate them. Recently, many conditions have been proposed and integrated into the GANs for various applications such as image segmentation [12]–[14], image synthesis [15], super-resolution [16], image

reconstruction [17]–[19], medical image translation [20]–[23], words to images synthesis [24], and object detection [25]. The conditional GANs are generally divided into paired image-to-image translation and unpaired image-to-image translation.

1) *Paired Image-to-image Translation*: The paired image-to-image translation methods obtain a mapping that converts an image from one domain to another by training on the paired datasets [12], [26]. Earlier, many paired image-to-image translation algorithms have been proposed in various tasks, e.g, super resolution [16], image segmentation [27]–[30], registration, denoising, etc. Isola *et al* proposed Pix2pix [12] which can be applied to general translation tasks. However, it is often difficult to obtain paired training data to train the network models.

2) *Unpaired Image-to-image Translation*: Unpaired methods materialize the unpaired image datasets, *i.e.*, for each sample in one dataset, there is no corresponding sample in the other dataset. Donahue *et al.* [31] established an unsupervised generative adversarial method named BiGAN, which uses feature learning and representation to translate the data. Zhu *et al.* proposed a cycle consistent adversarial network (Cycle-GAN) [32], which consists of forward and backward cycle models for unsupervised image-to-image translation tasks. Kim *et al.* invented DiscoGAN [33] to seek the relationship between source and target domains. Huang *et al.* proposed MUNIT [34], which separates input samples in contents and intensity distributions in the latent space and achieves translation by switching intensity distributions. Yan *et al.* [35] presented an improvement of CycleGAN, which reduces the domain gaps across vendors on cardiac images. Since unpaired methods do not require paired samples, these methods are more convenient for practical use and attract more attention for reducing domain gaps. These unpaired methods transfer the intensity distributions of domains and could reduce the domain gaps to a certain extent. However, existing methods only considered the intensity distribution difference due to intensity change while ignoring the structure change, which is often important in diagnosis for medical images.

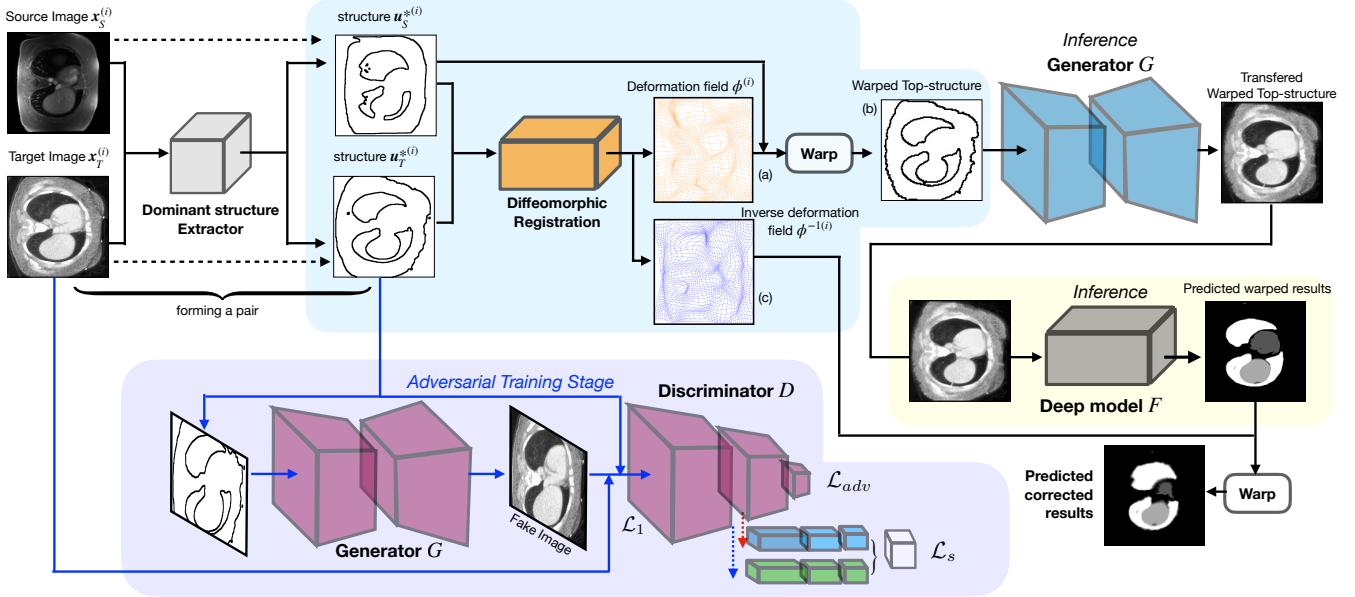


Fig. 3. The illustration of the model pipeline: Firstly, the source and target images ( $x_S^{(i)}$  and  $x_T^{(i)}$ ) are fed to a structure extraction model which computes the main dominant structure of the input image. Then, the obtained main structures  $u_S^{*(i)}$  and  $u_T^{*(i)}$  are used to compute the deformation field  $\phi^{(i)}$  and the inverse  $\phi^{-1(i)}$  in the diffeomorphic registration. The deformation field  $\phi^{(i)}$  is used to warp the  $u_S^{*(i)}$ , which is further processed by the generator  $G$ . The resultant image is fed to the trained segmentation model, whose output is warped back by the inverse deformation field  $\phi^{-1(i)}$  to get the final segmentation result.

### B. Diffeomorphic Image Registration

Image registration estimates a spatial deformation between a source (moving) image and a target (fixed) image, and the resultant spatial deformation can then warp the source image to the space that the target image lies. Among different registration approaches, diffeomorphism is an important feature which describes an invertible function that maps one differentiable deformation to another such that both the function and its inverse are differentiable [36]. Conventional iterative diffeomorphic registration methods such as LDDMM [36], Darte [37], ANTs [38], and Demons [39] are accurate but suffer from high computational costs. Very recently, Thorley *et al.* [40] proposed a fast iterative method based on the Nesterov accelerated ADMM for diffeomorphic registration, but its performance is limited for cross-domain problems. Building on the spatial transform network [41], the last few years have seen a boom in image registration methods based on deep learning. These include VoxelMorph [42], SYMNet [43], B-spline Network [44] and VR-Net [45], just to name a few. To achieve diffeomorphisms, most deep learning methods use multiple squaring and scaling as a neural layer [42]–[44]. However, these methods are designed without considering differences in intensity distributions.

## III. METHOD

In this paper, we propose an image translation approach such that an input image can be converted to an output image while the domain gaps in both intensity distribution and structure can be minimized. We define the set of test data for transfer as  $X_S$  and the set of training data with labelled segmentation ground truth as  $X_T$ . Our goal is to learn a mapping from  $X_S$  to  $X_T$ , such that the element

$x_S \sim P_{X_S}$  will be translated to  $x_T \sim P_{X_T}$  which has the same underlying structure and intensity distributions as in  $X_T$ . Since the objective of the intensity distribution transfer is to overcome the domain adaptation issue for subsequent analysis task such as segmentation, the content of the images or the underlying clean part of the images shall be kept unchanged. As shown in Fig. 3, we firstly use the structure extractor block to obtain the main dominant structure  $u^*$ . Then, we use it to generate a mask. An attention based diffeomorphic registration module is established to get the forward and inverse deformation fields ( $\phi$  and  $\phi^{-1}$ ) between the input and target images. After that, we utilise  $\phi$  to warp structure images  $u^*$  to get  $u^*(\phi)$ , which is fed into a structure-to-image rendering generator  $G$ . Finally, the outputs  $G(u^*(\phi))$  of  $G$  are expected to have similar structures and intensities as images in the target domain. Since the structures are deformed in the diffeomorphic registration module, we use the inverse deformation field  $\phi^{-1}$  to warp the segmentation outputs back to original state as final segmentation output. The intermediate results are illustrated in the Fig. 4.

### A. Dominant Structure Extractor

Firstly, we apply the the joint image reconstruction and segmentation Potts model [46] to obtain a basic clustering map  $u$  for input image  $x$ . The Potts problem is expressed as follows:

$$\min_u \left\{ \gamma \sum_{s=1}^S \omega_s \|\nabla^s u\|_0 + \|Au - x\|_2^2 \right\}, \quad (1)$$

where  $A$  is a matrix of ones,  $\nabla^s$  denotes the  $s^{th}$  order gradient,  $\|\nabla^s u\|_0$  represents the jump penalty,  $\|Au - x\|_2^2$

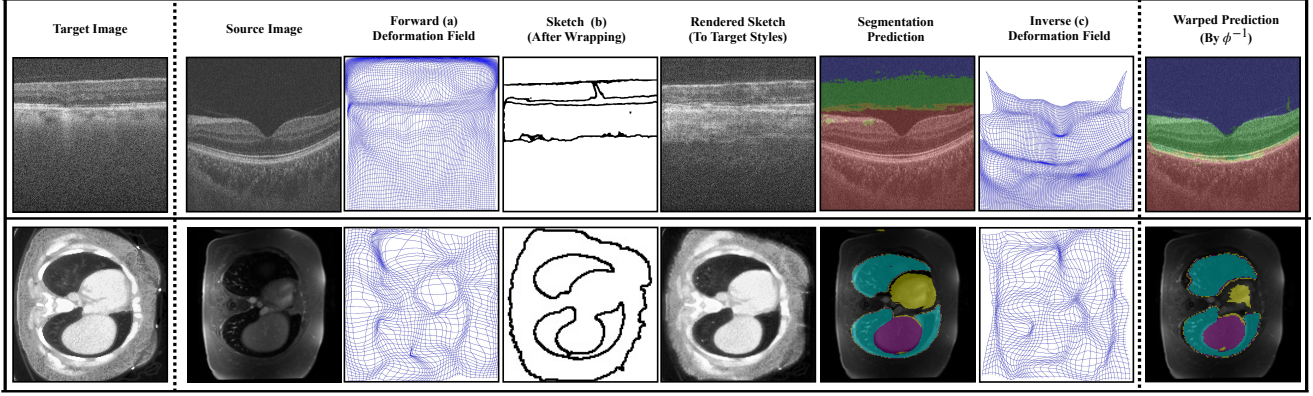


Fig. 4. The intermediate results in the pipeline. From left to right are target image  $x_T$ , source image  $x_S$ , the forward deformation field  $\phi$ , the warped top-structure  $u^*(\phi)$ , the rendered top-structure, the prediction results, the inverse deformation field  $\phi^{-1}$ , and the warped back prediction results. The notations (a), (b) and (c) correspond to the same notations in the Fig. 3.

represents the data fidelity,  $\gamma > 0$  denotes a hyper-parameter which controls the balance of two terms, and  $\omega_s$  denote hyper-parameters which balance different jump penalties. By solving this optimization problem, we obtain the clustering map  $u$ . Then its sketch  $u^*$  is obtained by applying Sobel edge detection.

### B. Attention Based Diffeomorphic Registration

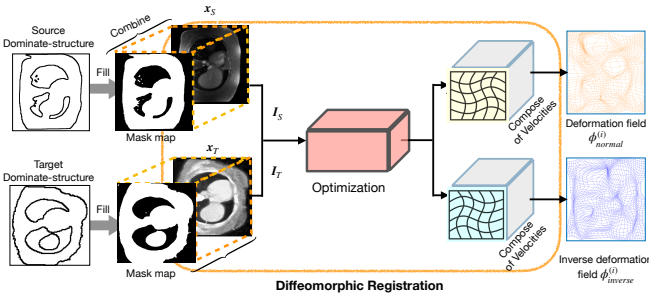


Fig. 5. Illustration of the registration procedure.

In order to generate images with structure similar to that in the target domain, we compute the deformation between  $u_s^*$  and  $u_t^*$ . This process aims to solve deformation  $\phi$  and the inverse  $\phi^{-1}$  between structures (which will be filled to become masks) from source and target domains rather than cross-modality image registration. Additionally, we composed the input images with our generated masks in this model.

As shown in Fig. 5, we fill the structures  $u_s$  to become mask maps by alternately assigning adjacent areas with black and white. Then these maps are combined with their correlated source images  $x_S$  and  $x_T$  to get the composed structure images  $I_S$  and  $I_T$ , i.e., we give the mask a Gaussian gradient and multiply it with its corresponding source image.

Given a pair of the composed structure images  $I_S$  and  $I_T$  (the pair with max SSIM score), we propose an invertible registration method to align them. Computing a diffeomorphic deformation can be treated as modelling a dynamical system [36], given by the ordinary differential equation (ODE):

$\partial\phi/\partial t = \mathbf{v}_t(\phi_t)$ , where  $\phi_0 = \text{Id}$  is the identity transformation and  $\mathbf{v}_t$  indicates the velocity field at time  $t \in [0, 1]$ . To solve the ODE, we use the Euler integration, in which the forward deformation field  $\phi$  is calculated from the compositions of a series of small deformations, defined as

$$\phi = \left(\text{Id} + \frac{\mathbf{v}_{t_{N-1}}}{N}\right) \circ \dots \circ \left(\text{Id} + \frac{\mathbf{v}_{t_1}}{N}\right) \circ \left(\text{Id} + \frac{\mathbf{v}_0}{N}\right). \quad (2)$$

The backward deformation can be computed reversely as

$$\phi^{-1} = \left(\text{Id} - \frac{\mathbf{v}_0}{N}\right) \circ \left(\text{Id} - \frac{\mathbf{v}_{t_1}}{N}\right) \circ \dots \circ \left(\text{Id} - \frac{\mathbf{v}_{t_{N-1}}}{N}\right). \quad (3)$$

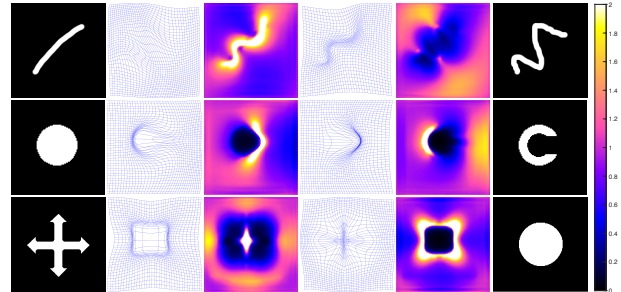


Fig. 6. Visualisations of diffeomorphic forward and backward (inverse) deformations. The first and the last columns show source image and target image respectively. The second and the fourth columns respectively show the forward and backward deformation fields. Finally, the third and the fifth columns show Jacobian determinants of corresponding forward and backward deformations.

In the above equations, if the velocity fields  $\mathbf{v}_{t_i}, \forall i \in \{0, \dots, N-1\}$  are sufficiently small whilst satisfying some smoothness constraint, the resulting compositions should result in a deformation that is diffeomorphic. In addition, note that the composition between  $\phi$  and  $\phi^{-1}$  will give an approximate identity grid and that one can use  $\phi^{-1}$  to warp an image back.

To compute the velocity fields whilst satisfying these diffeomorphic constraints, we use the following model

$$\min_{\mathbf{v}} \left\{ \frac{1}{2} \|\rho(\mathbf{v})\|^2 + \frac{\lambda}{2} \|\nabla^n \mathbf{v}\|^2 \right\}, \quad (4)$$

where  $\rho(\mathbf{v}) = \langle \nabla I_S, \mathbf{v} \rangle + I_S - I_T$ .  $\nabla^n$  denotes the  $n^{\text{th}}$  order gradient. We select  $n = 3$  since it gives a better

performance over gradients with other orders [40]. For a scalar-valued function  $f(x, y, z)$  in the continuous setting,  $\nabla^n f = [(k_1, k_2, k_3) \frac{\partial^2 f}{\partial x^{k_1} \partial y^{k_2} \partial z^{k_3}}]^T$ , where  $k_i = 0, \dots, n$ ,  $i \in \{1, 2, 3\}$  and  $k_1 + k_2 + k_3 = n$ . Moreover,  $(k_1, k_2, k_3)$  are known as multinomial coefficients which are computed by  $\frac{n!}{k_1!k_2!k_3!}$ . To solve the model effectively, we use a multi-scale ADMM algorithm developed in [40]. However, we note that our method improves upon [40] by adding a backward composition in order to compute the inverse transformation. An illustration of forward and inverse deformations are shown in the Fig. 6.

### C. Structure and Intensity Distribution Rendering Mapping

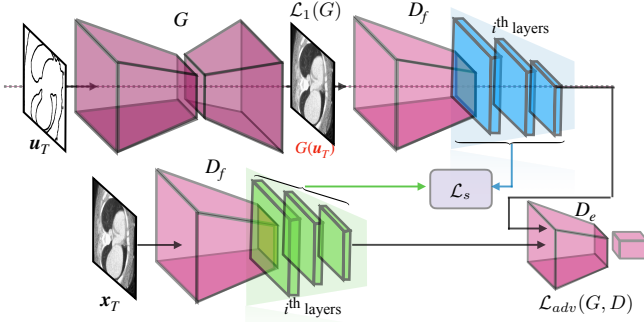


Fig. 7. Illustration of the structure rendering mapping Architecture, where,  $D_f$  and  $D_e$  denotes the start and the end parts of the discriminator  $D$ .

A structure and intensity distribution rendering module is proposed to render the warped structures to images with target intensity distributions. As shown in Fig. 7, it is a paired image-to-image translation network, including a ‘‘U-Net’’ [47] structure for the translation mapping, a discriminator for adversarial training and a feature alignment mechanism for loss computation. Mathematically, we compute the losses  $\mathcal{L}_{adv}$ ,  $\mathcal{L}_1$  and  $\mathcal{L}_s$  for the three components as follows:

$$\begin{aligned} \mathcal{L}_{adv} = & \mathbb{E}_{\mathbf{u}_T \sim U_T} [\log(1 - D(G(\mathbf{u}_T), \mathbf{u}_T))] \\ & + \mathbb{E}_{(\mathbf{x}_T, \mathbf{u}_T) \sim (X_T, U_T)} [\log D(\mathbf{x}_T, \mathbf{u}_T)], \end{aligned} \quad (5)$$

where  $\mathbf{u}_T \sim U_T$  represents the target structure images,  $(\mathbf{x}_T, \mathbf{u}_T) \sim (X_T, U_T)$  represents the target image and structure pair and  $D$  represents the discriminator of the mapping  $G$ .

$$\mathcal{L}_1 = \mathbb{E}_{(\mathbf{x}_T, \mathbf{u}_T) \sim (X_T, U_T)} \|G(\mathbf{u}_T) - \mathbf{x}_T\|_1, \quad (6)$$

where  $\|\cdot\|_1$  denotes the  $\ell_1$ -norm. Then feature correlations are given by Gram matrix  $Gr$ , where  $Gr(\mathbf{x}_T)_{ij}^{(l)}$  represents the  $l^{th}$  layer of feature maps of  $D$  with input  $\mathbf{x}_T$  and  $\mathbf{u}_T$ . It is computed as follows:

$$Gr(\mathbf{x}_T)_{ij}^{(l)} = \text{vec} \left[ \mathcal{F}(\mathbf{x}_T)_i^{(l)} \right]^T \text{vec} \left[ \mathcal{F}(\mathbf{x}_T)_j^{(l)} \right], \quad (7)$$

where  $\mathcal{F}(\mathbf{x}_T)_i^{(l)}$  represents the  $i^{th}$  layer of  $D$ 's feature maps, the subscripts  $i$  and  $j$  denotes the  $i^{th}$  and  $j^{th}$  maps,  $\text{vec}(\cdot)$  denotes the vectorization operation.

$$\mathcal{L}_s = \mathbb{E}_{(\mathbf{x}_T, \mathbf{u}_T) \sim (X_T, U_T)} \sum_{l=1}^3 \|Gr(G(\mathbf{u}_T))^{(l)} - Gr(\mathbf{x}_T)^{(l)}\|_F \quad (8)$$

The full objective of structure-rendering model is described as the following equation.

$$G^*, D^* = \arg \min_G \max_D [\mathcal{L}_{adv} + \lambda_1 \mathcal{L}_1 + \lambda_2 \mathcal{L}_s], \quad (9)$$

where  $\lambda_1$  and  $\lambda_2$  are hyper-parameters to control the balance of losses.

The optimization procedures of the whole model are summarized in Algorithm 1.

---

#### Algorithm 1: Optimization Procedures

---

**Input:**  $\mathbf{x}_S^{(i)} \in X_S$  and  $\mathbf{x}_T^{(i)} \in X_T$ .

**Require:**  $G$  and  $D$ . Two Adam optimizers  $A_1$  and  $A_2$ .

**for**  $epoch < N$  **do**

**for every**  $\mathbf{x}_T^{(i)} \in T$  **do**

    Obtain  $\mathbf{u}_T^{(i)}$  via (1);

    Calculate  $\mathcal{L}_{adv}(G, D)$ ,  $\mathcal{L}_s(G)$  and  $\mathcal{L}_1(G)$ ;

$D \leftarrow A_1(D, [\mathbf{x}_T^{(j)}, G(\mathbf{u}_T^{(i)})], \mathcal{L}_{adv})$ ;

$G \leftarrow A_2(D, [\mathbf{x}_T^{(j)}, G(\mathbf{u}_T^{(i)})], [\mathcal{L}_{adv}, \mathcal{L}_1, \mathcal{L}_s])$ ;

**end**

**if**  $epoch == N - 1$  **then**

**for every**  $\mathbf{x}_S^{(j)} \in S$  **do**

    obtain  $\mathbf{u}_S^{(i)}$  via (1);

    Calculate the SSIM of  $I_S^{(i)}$  and  $I_T^{(j)}$ ;

**end**

  Solve deformations  $\phi$  and  $\phi^{-1}$  for indexes of the pair has the max SSIM via (4);

**end**

**end**

**Return:**  $G$  and all deformations.

---

### D. Training Details

In the structure rendering part, we set hyper-parameter  $\lambda_1 = 1$  and  $\lambda_2 = 100$  in the equation (9) for all the translation experiments. We apply the Adam optimizer [49] with a learning rate of 0.0002 in all experiments, and the learning rate decays to zero following a linear principle from the 100<sup>th</sup> epoch to the 200<sup>th</sup> epoch. Moreover, the padding pixel number is 8, tolerance ratio is 0.001, the balance hyper-parameter is 5 and the max-iteration is 50 in the registration of all experiments. Additionally, we set the  $\gamma = 0.35$  for the OCT experiments and  $\gamma = 0.45$  for the MRI and CT experiments in equation (1).

## IV. EXPERIMENTAL RESULTS

### A. Domain Adaptation on Retinal OCT

1) *Datasets:* We first apply SUAM on retinal OCT to transfer the shape characteristics and intensity distribution of one OCT dataset to another. The SINA and ATLANTIS datasets are used for the retinal OCT experiments. The SINA dataset<sup>1</sup> contains 220 B-scans from 20 volumes of eyes with drusen and geographic atrophy, collected using a spectral domain-OCT imaging systems from Bioptigen. Three boundaries have been

<sup>1</sup>[https://people.duke.edu/~sf59/Chiu\\_IOVS\\_2011\\_dataset.htm](https://people.duke.edu/~sf59/Chiu_IOVS_2011_dataset.htm)

TABLE I  
SEGMENTATION EVALUATION OF RETINAL OCT

Methods	Distribution		Segmentation					
	$D_{Bhat} \downarrow$	$Corr \uparrow$	$mIoU \uparrow$	$Dice \uparrow$	$Acc \uparrow$	$Sen \uparrow$	$Spe \uparrow$	$FDR \downarrow$
Without Transfer	.391	.587	.420(.057)	.538(.060)	.854(.028)	.586(.056)	.891(.023)	.384(.027)
CycleGAN [32]	.139	.810	.497(.059)	.624(.058)	.875(.024)	.656(.065)	.909(.017)	.363(.052)
MUNIT [34]	<b>.071</b>	<b>.959</b>	.323(.032)	.422(.033)	.811(.021)	.439(.026)	.867(.014)	.529(.021)
DualGAN [48]	.313	.597	.390(.021)	.500(.024)	.839(.014)	.574(.018)	.881(.010)	.394(.012)
VoxelMorph [42]	.340	.369	.235(.015)	.324(.016)	.760(.013)	.400(.015)	.806(.006)	.533(.115)
VR-Net [45]	.237	.677	.240(.027)	.333(.036)	.761(.015)	.415(.031)	.812(.009)	.451(.058)
<b>Ours</b>	.109	.871	<b>.748(.024)</b>	<b>.813(.021)</b>	<b>.974(.006)</b>	<b>.850(.030)</b>	<b>.984(.003)</b>	<b>.202(.019)</b>

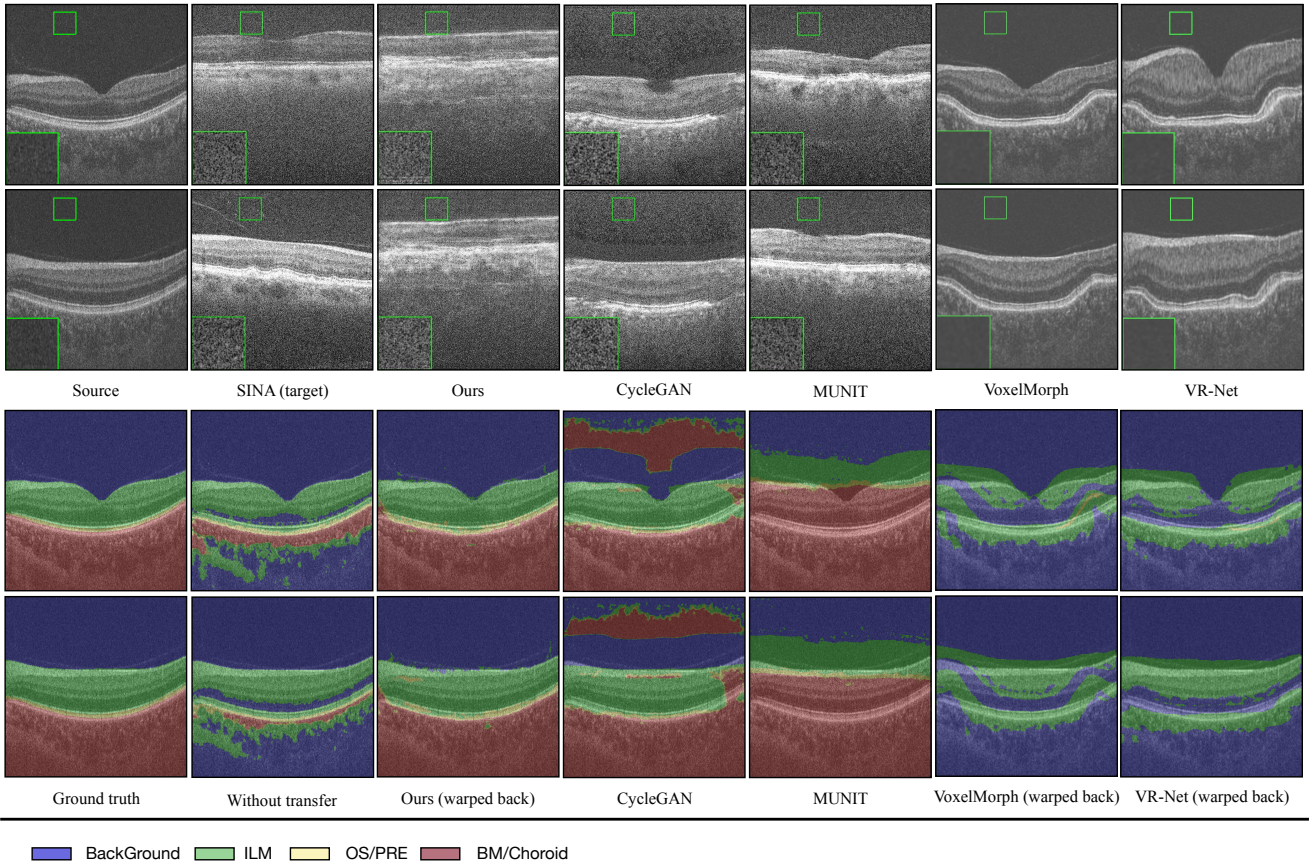


Fig. 8. Results of translated images in the OCT experiment. From top to down, each row locates a series of comparisons for a input sample. Particularly, the first and second rows show the intensity distribution translation results, the third and fourth rows represent the segmentation results.

manually annotated, including boundary 1: internal limiting membrane (ILM); boundary 2: between the outer segments and the retinal pigment epithelium (OS/RPE); and boundary 3: between Bruchs membrane and the choroid (BM/Choroid). We use this dataset as the target  $T$ . The ATLANTIS dataset is a local dataset, containing 176 B-scans, collected using a swept-source OCT machine. The same three boundaries as SINA are annotated. Since the two datasets are collected from different machines under different protocols, there exists gaps in both shape and intensity distributions, which makes the models trained from one dataset perform poorly on the other.

2) *Performance of Structure and intensity distribution Translation*: The performance of the image translation is evaluated in terms of both structure and intensity distribution.

**Evaluation on Structure Transfer**: The performance evaluation of the structure transfer is challenging. Ideally, it would be evaluated by comparing the translated image with the corresponding image from the other machine. However, it is not practical to image the exact same region of the eye using different machines. Since the main object of the translation is to improve subsequent analysis, we evaluate its performance with the segmentation layer indirectly.

A segmentation network based on the U-Net architecture is first trained using the SINA dataset. The proposed generative model is trained to translate ATLANTIS images such that the structure characteristics and intensity distributions are similar to those in SINA. The trained U-Net segmentation model is then applied on the translated data to detect the three boundaries, which are subsequently used to evaluate the performance of the image to image translation model.

The commonly used mean intersection-over-union ( $mIoU$ ) [50], the mean Sørensen–Dice coefficient ( $Dice$ ), the accuracy ( $Acc$ ), the sensitivity ( $Sen$ ), the specificity ( $Spe$ ), and the false discovery rate ( $FDR$ ) are used as evaluation metrics.

To evaluate the effectiveness of the proposed SUAM, we compare it with state-of-the-art translation methods including CycleGAN [32], MUNIT [34] and DualGAN [48] as well as the registration method VoxelMorph [42] and VR-Net [45]. In the experiments, we train these GANs in a similar way to learn the translation from ATLANTIS to SINA. The transferred ATLANTIS is then fed into the U-Net segmentation network to segment the three boundaries for comparison with the manual ground truth. For the registration methods, the deformation is computed to warp the image for segmentation. The output of the segmentation is warped back by the inverse deformation for comparison. TABLE I shows the comparison between the proposed method and other methods, where values are shown in the form of mean(std). As shown from the results, the proposed SUAM outperforms the state-of-the-art performance on all metrics.

Fig. 8 shows some sample results for visual comparison. As can be observed, Cycle-GAN indiscriminately transfers image content (intensity distribution and structure), resulted in a SINA-shaped segmentation input and prediction. Since the prediction is in a different domain than the input, we cannot forcibly apply SINA-to-ATLANTIS of Cycle-GAN and there is no displacement information as we obtained in our method. Therefore, the raw SINA-shaped prediction sees very low performance. This phenomena is more obvious on MUNIT which transfers the structure even better. Respectively, our method achieves a gain of 0.251 on  $mIoU$  and 0.189 on  $Dice$  compared to Cycle-GAN, and a gain of 0.425 on  $mIoU$  and 0.391 on  $Dice$  compared to MUNIT. DualGAN does not achieve desired segmentation performance because of two reasons. Firstly, they cannot differentiate the difference between structure and intensity distribution. Secondly, they suffer from the domain gap in shape which we tackled by the deformation in the proposed method. Our method achieves a gain of 0.358 on  $mIoU$  and 0.313 on  $Dice$  compared to DualGAN. Moreover, registration methods, *i.e.*, VoxelMorph and VR-Net, do not achieve acceptable results because they ignore the difference in texture and intensity distribution.

**Evaluation on intensity distribution Transfer:** We also evaluate the performance of intensity distribution translation from the SINA to ATLANTIS. Two metrics Bhattacharyya distance  $D_{Bhat}$  [51] and correlation  $Corr$  [52] are computed to evaluate the performance of intensity distribution transfer. To calculate the two metrics, we calculate the histograms of both transferred images and target images:

$$Corr(H_1, H_2) = \frac{\sum_I (H_1(I) - \bar{H}_1)(H_2(I) - \bar{H}_2)}{\sqrt{\sum_I (H_1(I) - \bar{H}_1)^2 \sum_I (H_2(I) - \bar{H}_2)^2}}, \quad (10)$$

$$D_{Bhat}(H_1, H_2) = \sqrt{1 - \frac{1}{\sqrt{\bar{H}_1 \bar{H}_2 N^2} \sum_I \sqrt{H_1(I) H_2(I)}}, \quad (11)$$

where  $H_1$  and  $H_2$  denote the normalized histograms.  $I$  denotes background regions,  $\bar{H}_k = \frac{1}{N} \sum_J H_k(J)$  represents the mean value of histogram  $H_k$ ,  $k = 1, 2$ , and  $N$  denotes the total number of histogram bins.

As shown in Fig. 8 and Table I, most GAN based methods could obtain good results on translating the intensity distributions. However, MUNIT cannot preserve the content information as it tends to change the structure to fit the target distribution, which seriously reduces the segmentation performance. CycleGAN achieves balanced results in shifting the intensities and keeping structural information, however, some unnatural shapes and structures appear. Although registration methods reduce the shape gap between source and target datasets, the structure differences still persist to a certain extent and the intensity difference cannot be conquered.

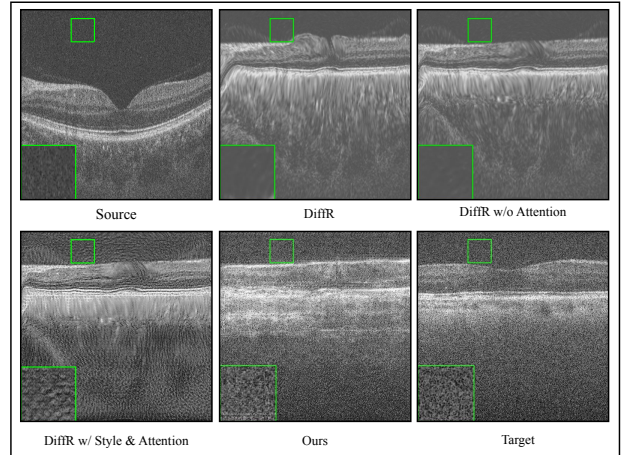


Fig. 9. Illustrations of translated results in ablation study

TABLE II  
RESULTS OF ABLATION STUDY.

Method	$mIoU \uparrow$	$Dice \uparrow$	$FDR \downarrow$
w/o transfer	.428	.547	.381
DiffR w/o Attention	.367	.504	.391
DiffR w/ Attention	.316	.445	.419
DiffR w/ Transfer	.305	.408	.430
DiffR w/ Transfer & Attention	.326	.438	.425
Ours	<b>.748</b>	<b>.813</b>	<b>.202</b>

3) *Ablation Study:* In order to justify each component of the proposed method, we conduct the following ablation studies. The following methods are compared: (1) The baseline approach is the direct use of the model trained on SINA without any other processing, denoted as w/o transfer. (2)

TABLE III  
SEGMENTATION EVALUATION OF CHEST MRI TO CT

Methods	Distribution		Segmentation					
	$D_{Bhat} \downarrow$	$Corr \uparrow$	$mIoU \uparrow$	$Dice \uparrow$	$Acc \uparrow$	$Sen \uparrow$	$Spe \uparrow$	$FDR \downarrow$
Without Transfer	.592	.043	.253(.006)	.337(.008)	.832(.003)	.325(.012)	.796(.004)	.635(.012)
CycleGAN [32]	.300	.314	.549(.073)	.683(.076)	.930(.014)	<b>.781</b> (.092)	.938(.024)	.343(.046)
MUNIT [34]	<b>.286</b>	<b>.407</b>	.517(.080)	.651(.086)	.924(.015)	.744(.104)	.929(.026)	.364(.055)
DualGAN [48]	.386	.102	.260(.010)	.348(.007)	.818(.004)	.358(.009)	.816(.012)	.635(.006)
VoxelMorph [42]	.371	.125	.314(.005)	.406(.009)	.859(.003)	.420(.012)	.834(.003)	.582(.013)
VR-Net [45]	.346	.135	.336(.012)	.441(.015)	.870(.004)	.507(.015)	.849(.005)	.557(.017)
<b>Ours</b>	.311	.291	<b>.618</b> (.045)	<b>.736</b> (.036)	<b>.958</b> (.006)	.723(.037)	<b>.945</b> (.009)	<b>.241</b> (.032)

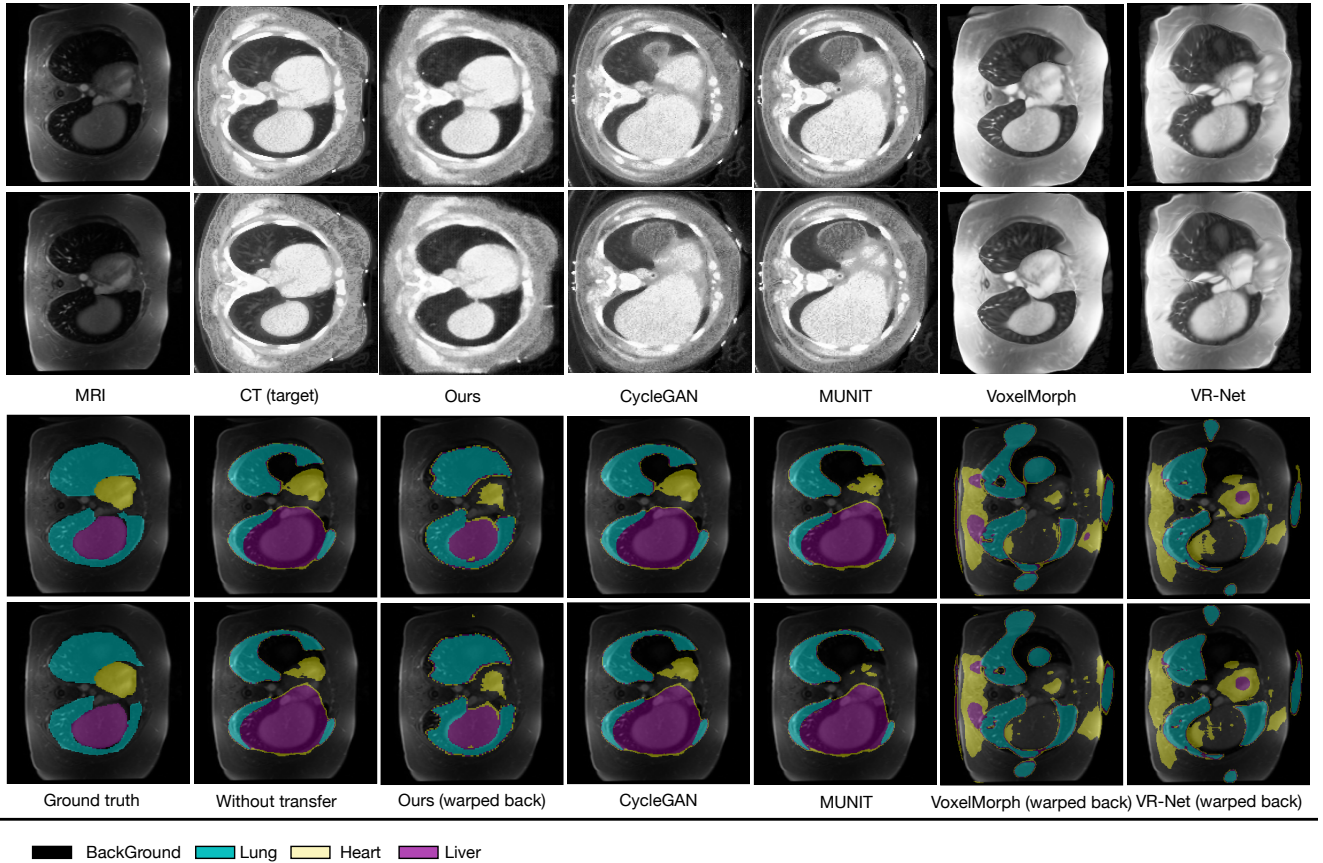


Fig. 10. Results of translated images in the MRI to CT experiment.

The proposed diffeomorphic registration method to warp AT-LANTIS images to SINA, denoted as DiffR w/o Attention. (3) The DiffR method with attention based mechanism, denoted as DiffR w/ Attention. (4) Apply intensity distribution translation method to the DiffR registration results, denoted as DiffR w/ Transfer. (5) The intensity distribution transfer method materialized to the DiffR method with Attention based routine (DiffR w/ Transfer & Attention). We show their performance in Table II.

Fig. 9 shows an example for visual comparison. As shown, if we only employ a registration method, we are unable to obtain an accurate deformation. By attaching the attention based mechanism, the registration results improve sig-

nificantly. However, there are still many distortions in the translated results, such as the line-shape noise patterns. Such distortions could lower the segmentation performance and can hardly be eased by intensity distribution translation methods. For example, source image warped by DiffR Attention and transferred intensity distributions by DualGAN still remains distorted. Because it is hard to separate these distortions from structure, the network might consider them as structures rather than intensity distribution.

### B. Domain Adaptation from MRI to CT

1) *Datasets*: Besides the domain transfer for single modality, SUAM is also applicable for multi-modalities. In the second

set of experiments, we apply the algorithms to transfer the shape characteristics and intensity distributions from MRI to CT. Two publicly available datasets<sup>2</sup> [53], [54] with manually labeled segmentation ground truth are used. The first dataset is a MRI dataset that includes three regions in the chest, *i.e.*, cardiac, lung and liver. The second dataset is a CT dataset, taken from the same patients as the MRI dataset and containing the same organs. We use the MRI dataset as the source  $X_S$  and the CT dataset as target  $X_T$ . In this experiment, we only use the common areas of 2D images in both modalities.

Cross modality translation often faces more comprehensive gaps in structure and intensity distribution. In some situations, the boundaries in the images can be fundamentally different because of the difference in imaging principles. For example, we observe gradually changing brightness from the center to the top and bottom in MRI, whereas, a close to uniform distribution is observed in CT. In addition, shape is more flat in MRI than CT.

Similar to retinal OCT domain adaptation, we train the segmentation network on CT and use it to infer MRI images which have been transferred to be CT-like. Similarly, the segmentation outputs are warped back and evaluated against the original MRI ground truth. We also compare the proposed method with other GAN based translation methods to assess how the transfer benefits the segmentation on MRI. Additionally, we scale the brightness of the MRI images for registration based methods to make a fair comparison, because they are sensitive to differences in intensity.

2) *Performance of Structure and intensity distribution Transfer:* Similar to that in retinal OCT evaluation, we also train a segmentation network and compare our method with GAN-like unsupervised domain adaptation methods and registration based methods.

**Evaluations of Structure Transfer:** We first evaluate the structure transfer from MRI to CT. As shown in the Table III and Fig. 10, our proposed SUAM outperforms the state-of-the-art methods on *mIoU*, *Dice*, *Acc*, *Spe* and *FDR*. Structures of cardiac, lung and liver are transferred successfully compared with the VR-net, Voxelmorph and DualGAN methods. While our inverse deformation can maintain the original shapes compare with translation GANs such as MUNIT and CycleGAN.

**Evaluations of Intensity Distribution Transfer:** We also evaluate the intensity distribution transfer. Table III compares the proposed method with other methods. Fig. 10 gives some examples for visual comparison. As shown in the results, translation GANs could also obtain good results on translating the intensity distributions similarly to the OCT experiment. Unsurprisingly, MUNIT achieves the best distribution results but obtains bad results in segmentation. This is reasonable as MUNIT changes the semantic information and leads to misaligned masks. Furthermore, we can see that the translated images by our method not only reach good results in distribution alignment but also capture the structure information by obtaining the inverse deformations. Although registration methods reduce the shape gap between source and target

datasets, the structure difference still remains to a certain extent and the intensity difference can not be conquered.

## V. CONCLUSION

Image to image translation is an essential task in machine learning, especially for tasks across different modalities. In this paper, we propose to reduce the domain shifts in both structure and intensity distribution. A novel SUAM which contains a structure extractor, an attention registration and a structure-rendering module, is proposed in this paper. Our experimental results have shown the effectiveness of the proposed framework. Our method, SUAM, is able to transfer both the structure and intensity distribution and improve segmentation results. Although our method achieves state-of-the-art performance, it does not work well for very small targets or lesions as they are often too small to be detected by the dominant structure extractor.

## REFERENCES

- [1] Y. Xu, T. Mo, Q. Feng, P. Zhong, M. Lai, I. Eric, and C. Chang, "Deep learning of feature representation with multiple instance learning for medical image analysis," in *Acoustics, Speech and Signal Processing (ICASSP)*. 2104 IEEE, 2014, pp. 1626–1630.
- [2] S. Adabi, E. Rashedi, A. Clayton, H. Mohebbi-Kalkhoran, X.-w. Chen, S. Conforto, and M. N. Avnani, "Learnable despeckling framework for optical coherence tomography images," *Journal of biomedical optics*, vol. 23, no. 1, p. 016013, 2018.
- [3] G. Litjens, T. Kooi, B. E. Bejnordi, A. A. A. Setio, F. Ciompi, M. Ghafoorian, J. A. Van Der Laak, B. Van Ginneken, and C. I. Sánchez, "A survey on deep learning in medical image analysis," *Medical image analysis*, vol. 42, pp. 60–88, 2017.
- [4] D. Shen, G. Wu, and H.-I. Suk, "Deep learning in medical image analysis," *Annual review of biomedical engineering*, vol. 19, pp. 221–248, 2017.
- [5] J. Donahue, Y. Jia, O. Vinyals, J. Hoffman, N. Zhang, E. Tzeng, and T. Darrell, "Decaf: A deep convolutional activation feature for generic visual recognition," in *International conference on machine learning*, 2014, pp. 647–655.
- [6] L. Duan, I. W. Tsang, and D. Xu, "Domain transfer multiple kernel learning," *IEEE Transactions on Pattern Analysis and Machine Intelligence*, vol. 34, no. 3, pp. 465–479, 2012.
- [7] M. Long, H. Zhu, J. Wang, and M. I. Jordan, "Deep transfer learning with joint adaptation networks," in *Proceedings of the 34th International Conference on Machine Learning-Volume 70*. JMLR. org, 2017, pp. 2208–2217.
- [8] C. Chen, C. Ouyang, G. Tarroni, J. Schlemper, H. Qiu, W. Bai, and D. Rueckert, "Unsupervised multi-modal style transfer for cardiac mr segmentation," in *International Workshop on Statistical Atlases and Computational Models of the Heart*. Springer, 2019, pp. 209–219.
- [9] T. Zhang, J. Cheng, H. Fu, Z. Gu, Y. Xiao, K. Zhou, S. Gao, R. Zheng, and J. Liu, "Noise adaptation generative adversarial network for medical image analysis," *IEEE transactions on medical imaging*, vol. 39, no. 4, pp. 1149–1159, 2019.
- [10] I. Goodfellow, J. Pouget-Abadie, M. Mirza, B. Xu, D. Warde-Farley, S. Ozair, A. Courville, and Y. Bengio, "Generative adversarial nets," in *Advances in neural information processing systems*, 2014, pp. 2672–2680.
- [11] E. L. Denton, S. Chintala, R. Fergus *et al.*, "Deep generative image models using a laplacian pyramid of adversarial networks," in *Advances in neural information processing systems*, 2015, pp. 1486–1494.
- [12] P. Isola, J.-Y. Zhu, T. Zhou, and A. A. Efros, "Image-to-image translation with conditional adversarial networks," in *Proceedings of the IEEE conference on computer vision and pattern recognition*, 2017, pp. 1125–1134.
- [13] P. Luc, C. Couprie, S. Chintala, and J. Verbeek, "Semantic segmentation using adversarial networks," in *NIPS Workshop on Adversarial Training*, 2016.

<sup>2</sup><https://learn2reg.grand-challenge.org>

- [14] Q. Dou, C. Ouyang, C. Chen, H. Chen, and P.-A. Heng, "Unsupervised cross-modality domain adaptation of convnets for biomedical image segmentations with adversarial loss," in *IJCAI International Joint Conference on Artificial Intelligence*, 2018, p. 691.
- [15] H. Kazemi, M. Iranmanesh, A. Dabouei, S. Soleymani, and N. M. Nasrabadi, "Facial attributes guided deep sketch-to-photo synthesis," in *2018 IEEE Winter Applications of Computer Vision Workshops (WACVW)*. IEEE, 2018, pp. 1–8.
- [16] C. Ledig, L. Theis, F. Huszár, J. Caballero, A. Cunningham, A. Acosta, A. Aitken, A. Tejani, J. Totz, Z. Wang *et al.*, "Photo-realistic single image super-resolution using a generative adversarial network," in *Proceedings of the IEEE conference on computer vision and pattern recognition*, 2017, pp. 4681–4690.
- [17] J. M. Wolterink, A. M. Dinkla, M. H. Savenije, P. R. Seevinck, C. A. van den Berg, and I. Išgum, "Deep mr to ct synthesis using unpaired data," in *International workshop on simulation and synthesis in medical imaging*. Springer, 2017, pp. 14–23.
- [18] J. M. Wolterink, T. Leiner, M. A. Viergever, and I. Išgum, "Generative adversarial networks for noise reduction in low-dose ct," *IEEE transactions on medical imaging*, vol. 36, no. 12, pp. 2536–2545, 2017.
- [19] Y. Wang, B. Yu, L. Wang, C. Zu, D. S. Lalush, W. Lin, X. Wu, J. Zhou, D. Shen, and L. Zhou, "3d conditional generative adversarial networks for high-quality pet image estimation at low dose," *Neuroimage*, vol. 174, pp. 550–562, 2018.
- [20] H. Zhao, H. Li, S. Maurer-Stroh, and L. Cheng, "Synthesizing retinal and neuronal images with generative adversarial nets," *Medical image analysis*, vol. 49, pp. 14–26, 2018.
- [21] T. Iqbal and H. Ali, "Generative adversarial network for medical images (mi-gan)," *Journal of medical systems*, vol. 42, no. 11, p. 231, 2018.
- [22] K. Armanious, C. Jiang, M. Fischer, T. Küstner, T. Hepp, K. Nikolaou, S. Gatidis, and B. Yang, "Medgan: Medical image translation using gans," *Computerized Medical Imaging and Graphics*, vol. 79, p. 101684, 2020.
- [23] K. Armanious, C. Jiang, S. Abdulatif, T. Küstner, S. Gatidis, and B. Yang, "Unsupervised medical image translation using cycle-medgan," in *2019 27th European Signal Processing Conference (EUSIPCO)*. IEEE, 2019, pp. 1–5.
- [24] S. Reed, Z. Akata, X. Yan, L. Logeswaran, B. Schiele, and H. Lee, "Generative adversarial text to image synthesis," in *International Conference on Machine Learning*, 2016, pp. 1060–1069.
- [25] C. Xie, J. Wang, Z. Zhang, Y. Zhou, L. Xie, and A. Yuille, "Adversarial examples for semantic segmentation and object detection," in *Proceedings of the IEEE International Conference on Computer Vision*, 2017, pp. 1369–1378.
- [26] S. Tripathy, J. Kannala, and E. Rahtu, "Learning image-to-image translation using paired and unpaired training samples," *arXiv preprint arXiv:1805.03189*, 2018.
- [27] B. Lei, Z. Xia, F. Jiang, X. Jiang, Z. Ge, Y. Xu, J. Qin, S. Chen, T. Wang, and S. Wang, "Skin lesion segmentation via generative adversarial networks with dual discriminators," *Medical Image Analysis*, vol. 64, p. 101716, 2020.
- [28] Y. Xue, T. Xu, H. Zhang, L. R. Long, and X. Huang, "Segan: Adversarial network with multi-scale l1 loss for medical image segmentation," *Neuroinformatics*, vol. 16, no. 3, pp. 383–392, 2018.
- [29] Y. Zhang, L. Yang, J. Chen, M. Fredericksen, D. P. Hughes, and D. Z. Chen, "Deep adversarial networks for biomedical image segmentation utilizing unannotated images," in *International conference on medical image computing and computer-assisted intervention*. Springer, 2017, pp. 408–416.
- [30] X. Zhuang and J. Shen, "Multi-scale patch and multi-modality atlases for whole heart segmentation of mri," *Medical image analysis*, vol. 31, pp. 77–87, 2016.
- [31] J. Donahue, P. Krähenbühl, and T. Darrell, "Adversarial feature learning," in *International Conference on Learning Representations*, May 2016.
- [32] J.-Y. Zhu, T. Park, P. Isola, and A. A. Efros, "Unpaired image-to-image translation using cycle-consistent adversarial networks," in *2017 IEEE International Conference on Computer Vision (ICCV)*. IEEE, 2017, pp. 2242–2251.
- [33] T. Kim, M. Cha, H. Kim, J. K. Lee, and J. Kim, "Learning to discover cross-domain relations with generative adversarial networks," in *Proceedings of the 34th International Conference on Machine Learning—Volume 70*. JMLR. org, 2017, pp. 1857–1865.
- [34] X. Huang, M.-Y. Liu, S. Belongie, and J. Kautz, "Multimodal unsupervised image-to-image translation," in *Proceedings of the European conference on computer vision (ECCV)*, 2018, pp. 172–189.
- [35] W. Yan, Y. Wang, S. Gu, L. Huang, F. Yan, L. Xia, and Q. Tao, "The domain shift problem of medical image segmentation and vendor-adaptation by unet-gan," in *International Conference on Medical Image Computing and Computer-Assisted Intervention*. Springer, 2019, pp. 623–631.
- [36] M. F. Beg, M. I. Miller, A. Trouvé, and L. Younes, "Computing large deformation metric mappings via geodesic flows of diffeomorphisms," *International journal of computer vision*, vol. 61, no. 2, pp. 139–157, 2005.
- [37] J. Ashburner, "A fast diffeomorphic image registration algorithm," *Neuroimage*, vol. 38, no. 1, pp. 95–113, 2007.
- [38] B. B. Avants, N. J. Tustison, G. Song, P. A. Cook, A. Klein, and J. C. Gee, "A reproducible evaluation of ants similarity metric performance in brain image registration," *Neuroimage*, vol. 54, no. 3, pp. 2033–2044, 2011.
- [39] T. Vercauteren, X. Pennec, A. Perchant, and N. Ayache, "Diffeomorphic demons: Efficient non-parametric image registration," *NeuroImage*, vol. 45, no. 1, pp. S61–S72, 2009.
- [40] A. Thorley, X. Jia, H. J. Chang, B. Liu, K. Bunting, V. Stoll, A. de Marvao, D. P. O'Regan, G. Gkoutos, D. Kotecha *et al.*, "Nesterov accelerated admm for fast diffeomorphic image registration," in *International Conference on Medical Image Computing and Computer-Assisted Intervention*. Springer, 2021, pp. 150–160.
- [41] M. Jaderberg, K. Simonyan, A. Zisserman *et al.*, "Spatial transformer networks," in *Advances in Neural Information Processing Systems*, 2015, pp. 2017–2025.
- [42] A. V. Dalca, G. Balakrishnan, J. Guttag, and M. R. Sabuncu, "Unsupervised learning for fast probabilistic diffeomorphic registration," in *International Conference on Medical Image Computing and Computer-Assisted Intervention*. Springer, 2018, pp. 729–738.
- [43] T. C. Mok and A. C. Chung, "Fast symmetric diffeomorphic image registration with convolutional neural networks," in *IEEE/CVF Conference on Computer Vision and Pattern Recognition (CVPR)*, June 2020.
- [44] H. Qiu, C. Qin, A. Schuh, K. Hammernik, and D. Rueckert, "Learning diffeomorphic and modality-invariant registration using b-splines," in *Medical Imaging with Deep Learning*, 2021.
- [45] X. Jia, A. Thorley, W. Chen, H. Qiu, L. Shen, I. B. Styles, H. J. Chang, A. Leonardi, A. De Marvao, D. P. O'Regan *et al.*, "Learning a model-driven variational network for deformable image registration," *IEEE Transactions on Medical Imaging*, vol. 41, no. 1, pp. 199–212, 2021.
- [46] M. Storath, A. Weinmann, J. Frikel, and M. Unser, "Joint image reconstruction and segmentation using the potts model," *Inverse Problems*, vol. 31, no. 2, p. 025003, 2015.
- [47] O. Ronneberger, P. Fischer, and T. Brox, "U-net: Convolutional networks for biomedical image segmentation," in *International Conference on Medical image computing and computer-assisted intervention*. Springer, 2015, pp. 234–241.
- [48] Z. Yi, H. Zhang, P. Tan, and M. Gong, "Dualgan: Unsupervised dual learning for image-to-image translation," in *Proceedings of the IEEE international conference on computer vision*, 2017, pp. 2849–2857.
- [49] D. P. Kingma and J. Ba, "Adam: A method for stochastic optimization," *arXiv preprint arXiv:1412.6980*, 2014.
- [50] A. Khoreva, R. Benenson, J. Hosang, M. Hein, and B. Schiele, "Simple does it: Weakly supervised instance and semantic segmentation," in *Proceedings of the IEEE conference on computer vision and pattern recognition*, 2017, pp. 876–885.
- [51] A. Bhattacharyya, "On a measure of divergence between two statistical populations defined by their probability distributions," *Bulletin of the Calcutta Mathematical Society*, vol. 35, pp. 99–109, 1943.
- [52] R. C. Gonzalez and R. E. Woods, *Digital Image Processing (3rd Edition)*. Upper Saddle River, NJ, USA: Prentice-Hall, Inc., 2006.
- [53] A. D. Leow, I. Yanovsky, M.-C. Chiang, A. D. Lee, A. D. Klunder, A. Lu, J. T. Becker, S. W. Davis, A. W. Toga, and P. M. Thompson, "Statistical properties of jacobian maps and the realization of unbiased large-deformation nonlinear image registration," *IEEE transactions on medical imaging*, vol. 26, no. 6, pp. 822–832, 2007.
- [54] S. Kabus, T. Klinder, K. Murphy, B. van Ginneken, C. Lorenz, and J. P. Pluim, "Evaluation of 4d-ct lung registration," in *International Conference on Medical Image Computing and Computer-Assisted Intervention*. Springer, 2009, pp. 747–754.